Nanoscale

Accepted Manuscript

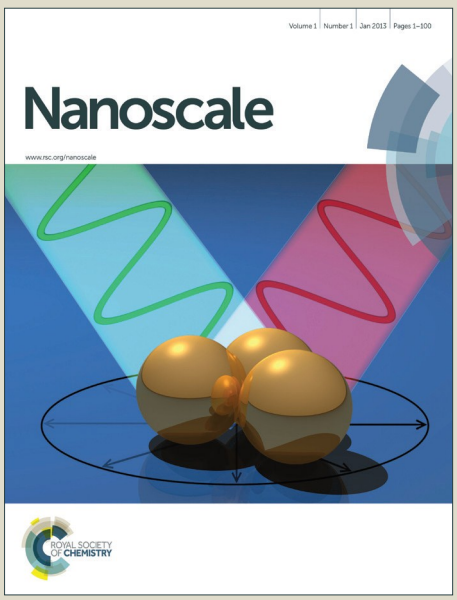

ROYAL SOCIETY OF CHEMISTRY

www.rsc.org/nanoscale

MOF-Derived N-doped Hierarchically Porous Carbon Sponges As Immobilizer to Confine Selenium as Cathodes for Li-Se Batteries with Superior Storage Capacity and Perfect Cycling Stability

Zhaoqiang Li, Longwei Yin*

Key Laboratory for Liquid-Solid Structural Evolution and Processing of Materials, Ministry of Education, School of Materials Science and Engineering, Shandong University, Jinan 250061, P. R. China

*To whom correspondence should be addressed. Tel.: + 86 531 88396970. Fax: + 86 531 88396970. E-mail: yinlw@sdu.edu.cn

Abstract Nitrogen-doped carbon sponges (NCS) composed of hierarchically micropores carbon layers, are derived from metal organic framework (MOF) via carbonization at high temperature under Ar and NH_3 flow. Se is impregnated into 0.4~0.55 nm micropores by melting-diffusion and infiltration method. The confinement of Se within small sized micropores of NCS efficiently avoids Se loss, mesopores between carbon layers absorb sufficient electrolyte, as well as serve as cushion space for the large volume change during delithiation-lithiation processes. Nitrogen doping improves the electric conductivity of carbon matrix and facilitates the fast charge transfer, making the carbon sponge a highway for charges involved in redox reactions. When acting as cathode materials for Li-Se batteries, the NCS/Se-50 composite with 50 wt.% Se exhibits excellent cycling stability, superior rate capability and high coulombic efficiency. The cathode can exhibit 443.2 mAh g^{-1} at the 200^{th} cycle with a coulombic efficiency up to 99.9% at 0.5 C (C= 675 mAh g^{-1}), leading to 0.031% capacity loss per cycle during 5^{th} to 200^{th} cycle. Even at high rate of 5 C, it can still retain 286.6 mAh g^{-1}. The unique large surface rod-like MOF derived N-doped carbon sponges with hierarchical pores could be potential candidates in the related energy-storage systems.

KEY WORDS: metal organic framework; micorpores; cathode; electrochemical performance; lithium-selenium battery

1. Introduction

The increasing demand for higher energy density storage devices steers scientific researches on high capacity electrode materials.[1-3] Duo to the relatively low theoretical capacity of commercial cathode materials for lithium-ion batteries, it's of great urgency to develop new generation cathode materials which should satisfy the request for high capacity and long cycle life.[4-6] Recently, lithium-sulfur (Li-S) batteries have attracted much attention owing to its high theoretical capacity (1672 mAh g^{-1}) and natural abundance[7]. Although much progress has been made, sulfur cathode still face limitations for its industrial-scale application because of its natural insulating property and the shuttle effect resulted form high-order polysulfide intermidiates.[8-10]

Selenium (Se) recently draws much attention for its advantage as cathode material for lithium-selenium (Li-Se) batteries. Se has a similar (de)lithiation mechanism to sulfur just as following reaction of $2Li^+ + Se + 2e^- \leftrightarrow Li_2Se$,[11] corresponding to a gravimetric capacity of 675 mAh g^{-1}, which is much lower than that of sulfur. However, owing to its high density (4.2 g cm^{-3}), Se provides a theoretical volumetric capacity density of 3253 mAh cm^{-3}, which is comparable to that of sulfur (3467 mAh cm^{-3})[12, 13]. Moreover, Se is one kind of metalloids, exhibiting much higher electric conductivity (1×10^{-3} S m^{-1}) than that of sulfur (5×10^{-28} S m^{-1})[11], which promises activated electrochemical reaction during delithiation-lithiation processes. Though its metalloid nature, it's still necessary to improve its electric conductivity. Also, the large volume change generated during delithiation-lithiation processes for Li-Se battery also needs to be accommodated and alleviated. To firmly confine Se to prevent its escaping and dissolution, an effective immobilizer with abundant hierarchically pores and large surface area and good electrical conductivity is needed to obtain superior electrochemical performance.

One efficient way to solve these problems is to combine Se with conductive carbon and polymer materials. Carbon materials not only provide an unhindered passway for the electrons, but also serve as buffer layer to alleviate volume changes. For example, Guo generated an advanced selenium-carbon cathode by confining Se_8 molecules in ordered mesopores of CMK-3, exhibiting good electrochemical performance.[12] Se_8 is confined in the mesopores of carbon sphere at 600 ºC under vacuum by Wang et al.,[14], promising fully reaction with Li and obtaining improved performance. Micropore-rich carbon nanospheres are used to confine Se as cathode material by Huang et al., and a protective film is formed on the surface to ensure its electrochemical performance stability for Li-Se battery.[15] Recently, it is shown that nitrogen doping makes a great contribution to the excellent electrochemical performance[16-18], which may also be applicable to Se cathode. Carbon materials derived from metal organic frameworks (MOF) have attracted much attention due to their large specific surface area, uniquely porous structure and microstructure controllability, showing excellent performance in hydrogen uptake[19], supercapacitor electrodes[20], sensing[21] and Li-S batteries[22]. The controllable synthesis of MOF derived n-doped

large surface carbon with abundant micropores and mespores, and confining Se in porous MOF-derived N-doped carbon as cathode for Li-Se battery with superior electrochemical performance is of great importance and challenging.

Herein, a nitrogen-doped carbon rod-like sponge (NCS) with abundant mesopores and micropores is derived from one kind of Al-MOF. The unique NCS sponge consists of interconnected rich-micropores (0.4~0.55 nm) in carbon layers and mesopores existing between carbon layers. Se can be firmly confined in micropores of NCS by a melting-diffusion and infiltration route to form NCS/Se composite, displaying excellent electrochemical performance as cathode for Li-Se batteries. The small sized micropores in carbon layers behave as a stable immobilizer for highly dispersed Se molecules, ensuring a short diffusion path of Li^+ ions, and the mesopores between carbon layers not only guarantee sufficient contact between active material and electrolyte but also provide redundant space to buffer volume changes. Nitrogen doping further facilitates the charge transfer during discharge/charge processes, resulting in excellent electrochemical performance, such as cycle stability, storage capacity and rate capability.

2. Experimental section

2.1 Preparation of nitrogen-doped carbon sponge (NCS) and NCS/Se composites

All the chemical reagents used in this work were used without further purification. The nitrogen-doped layered carbon sponge was prepared using a rod-like Al-MOF as the precursor.[23] Then the as-synthesized rod-like Al-MOF was heated at 800 ºC for 3 h with a heating rate of 5 ºC/min under Ar flow, followed by two more hours under the transformed NH_3 flow. The resultant black powders were then immersed into 10% HF aqueous solution to remove the Al species. After washed with deionized water and alcohol for several times, the nitrogen-doped rod-like carbon sponge (NCS) was obtained. For the carbon without nitrogen doping, the precursor was simply heated at 800 ºC under Ar for 5h.

1:1 and 2:1 weight ratio mixtures of bulk Se and NCS were thoroughly mixed in an agate mortar. Then the mixture was sealed in a glass tube under vacuum, and then heated at 260 ºC with a heating rate of 5 ºC/min for 20 h in a tube furnace. After cooling down to room temperature, the NCS/Se composites were obtained. TGA tests confirm the content of selenium is 50% and 60%, respectively, and the composites are denoted as NCS/Se-50, NCS/Se-60, respectively. For comparisons, the composites of Se and carbon sponge (CS) without nitrogen doping are denoted as CS/Se-50, CS/Se-60, respectively.

2. 2 Materials characterization

X-ray diffraction (XRD) patterns were collected using Rigaku D/Max-Rb diffractometer equipped with Cu Ka

radiation (λ = 1.5406 Å). The morphology and components of the synthesized products were analyzed using SU-70 field emission scanning electron microscopy (FE-SEM) and attached X-ray energy dispersive spectrometry (EDS), respectively. The microstructures of the synthesized products were analyzed using high-resolution transmission electron microscopy (HR-TEM) of JEM-2100 at an acceleration voltage of 200 kV. Nitrogen adsorption-desorption isotherms were determined at 77 K using Gold APP Vsorb 2800P surface area and porosity 60 analyzer. Raman spectra were measured and collected using a 632.8 nm laser with a JY HR800 under ambient conditions, with a laser spot size of about 1 μm. X-ray photoelectron spectroscopy (XPS) characterization was carried out in an ESCALAB 250 instrument with 150W Al Ka probe beam.

2.3 Electrochemical measurements

The electrochemical measurements were carried out by using 2025 coin-type cells, in which the C/Se composites as working electrode, a lithium metal foil with size of 15.8 × 0.2 mm as reference electrode, a celgard 2325 as separator and a solution of 1.0 M $LiPF_6$ in mixed EC and DEC (1:1 by volume) as the electrolyte. The C/Se composite cathode slurry was made by mixing 80 wt.% C/Se composite material, 10 wt.% LA132 (Indigo, China) binder and 10 wt.% ethylene carbonate in deionized water. After stirring for several hours, the slurry was spread onto 20 μm aluminum foil, which was followed by drying treatment at 60 ºC under vacuum overnight. The dried electrode was punched into round discs. Fresh coin cells were assembled in an Ar-filled glove box. The cell were discharged and charged on LAND CT2001A battery test system from 3.0 V to 1.0 V under 25 ºC. Cyclic Voltammetry (CV) and electrochemical impedance spectroscopy measurements were carried out on an electrochemical workstation (PARSTAT 2273) at room temperature.

3. Results and discussions

The morphology of the as-synthesized precursor Al-MOF is investigated using scanning electron microscopy (SEM). Figure S1 reveals rod-like products with square sectional morphology and smooth surfaces. After carbonization at 800 ºC and removal of Al species, the obtained nitrogen-doped carbon materials maintain structure of square rod-like sponge structures consisting of interconnected porous carbon layers (Fig. 1a-1b). The nitrogen-doped and pure porous carbon sponge products are denoted as NCS and CS samples, respectively. A typical high-magnification TEM image (Fig. 1c) further shows that the prepared NCS displays an interconnected layered sponge characteristic. HRTEM image (Fig. 1d) demonstrates the presence of disordered micropores in the NCS materials. The X-ray photoelectron spectroscopy (XPS) survey spectrum (Fig. 1e) shows a peak at 400 eV, corresponding to that of N 1s. The content of nitrogen is calculated to be 7.3 wt.%. The textural property of the NCS is examined by nitrogen adsorption-desorption measurements. As is shown in the nitrogen

adsorption-desorption isotherm (Fig. 2g), an approximately vertical rise of the isotherm at low pressure range (P/P_0~0) appears, suggesting the presence of typical micropores. [24] The hysteresis loop at P/P_0 of 0.4~0.99 derives from some mesopores, [25, 26] which is actually the space between the carbon layers. The micropore size distribution curve (Fig. 2h) reveals a narrow distribution of 0.4~0.55 nm, further confirming the existence of micropores. The broad distribution of 3~10 nm in the mesopore size distribution (Fig. 2i) confirms the existence of mesopores. The synthesized NCS exhibits an extremely large specific surface area of 1274.5 m^2 g^{-1}, a micropore volume of 0.358 cm^3 g^{-1} and a mesopore volume of 0.755 cm^3 g^{-1}. It should be promising for Se immobilization for cathode materials for Li-Se battery. The micropores can be used to confine Se species and meanwhile the mesopores can ensure sufficient contact with electrolyte.

To fabricate NCS/Se composite, a facile melting-diffusion infiltration process from a mixture of NCS and bulk selenium is used. SEM and TEM images of the NCS/Se-50 composite are shown in Fig. 2. After the heat treatment, no pristine bulk selenium can be found on the surface of composite (Fig. 2a-2b), demonstrating that Se has completely diffused into the pores of NCS. Elemental mapping image corresponding to SEM image in Fig. 2c (Fig. 2f) further confirms that Se is uniformly distributed in the NCS. A low-magnification TEM image in Fig. 2d shows the microstructures of the NCS/Se-50 composites. The NCS carbon structure is highly reserved after the diffusion of Se. The difference between HRTEM images for NCS (Fig. 1d) and NCS/Se-50 composite (Fig. 2e) can be detected. Se presents in the form of linear shape in the 0.4~0.55 nm micropores of NCS. The selected area electron diffraction (SAED) pattern (Fig. S3) shows the amorphous state for both C and Se. After Se is incorporated in NCS, the specific surface area of NCS/Se decreases from 1274.5 m^2g^{-1} for NCS to 195.2 m^2g^{-1} for NCS/Se-50 composite, indicates that Se occupies pores of the NCS sponge. Furthermore, the huge decrease of micropore volume from 0.358 cm^3g^{-1} to only 0.037 cm^3g^{-1} proves that Se is infused into the micropores of the NCS (Fig. 2g-2i). The small vertical rise of the isotherm at low pressure range (P/P_0~0) also confirms the existence of redundant micropores. The mesopore volume decreases from 0.755 cm^3g^{-1} to 0.351 cm^3g^{-1}. The mesopores in the NCS guarantee a sufficient contact between selenium and electrolyte, thus ensuring a fast mass transfer during discharge-charge processes. Furthermore, the redundant mesoporous and microporous space that isn't occupied by Se can effectively provide a space to buffer the volume changes during the discharge-charge processes. For the NCS/Se-60 sample, it exhibits a specific surface area of 24.9 m^2 g^{-1}, with micropore volume of 0 and mesopore volume of 0.166 cm^3g^{-1}. This indicates that all the micropores are filled with amorphous linear selenium, and even some mesopores are occupied by amorphous selenium.

Thermogravimetric analysis (TGA) of the NCS/Se composites is conducted in Ar flow to determine the selenium content and the mechanism of Se confinement in micropores. Since weight loss is derived from the

evaporation of selenium, the TGA pattern is also an effective indication of Se absorption strength in carbon micropores.[27] As is shown in Fig. 3a, a total weight loss of approximately 50% occurs during the heat treatment for the NCS/Se-50 sample. There is only one Se evaporation peak shown in Fig. 3a, indicating only one form of Se exists. Weight loss starts at 350 ºC, reaches its fastest loss speed at 510 ºC, and finally ends at 550 ºC. Se evaporation temperature in the 0.4~0.55 nm micropores of this NCS is higher than that in the carbon nanotubes[28], micro-mesoporous carbon[29] and even 1.1 nm microporous carbon[30], which may indicate a relatively higher absorption strength of 0.4~0.55 nm micropores against Se. For the NCS/Se-60 sample, it displays a weight loss of 60 wt.% of this composite, demonstrating a 60 wt.% content of selenium in the NCS/Se-60 composite. However, a relatively lower evaporation peak can be observed at 400 ºC, indicating the less stability of selenium in mesopores. This agrees well with the BET result.

Fig. 3b presents XRD patterns of pure CS, pristine bulk Se and NCS/Se-50 composite. For pristine bulk Se sample, diffraction peaks of crystalline selenium located at 23.5º (100), 29.7º (101), 41.3º (110), 43.6º (102), 45.4º (111), 51.7º (201), 55.7º (003), 61.6º (202) and 65.2º (210) can clearly be indexed to trigonal Se (JCPDS 06-0362). For pure CS, the broad diffraction peak at 24º of the carbon sponge can be associated with partially graphitized carbon[31]. However, after heat treatment on the mixture of Se and NCS, all the sharp diffraction peaks of the crystalline Se disappear, suggesting that selenium exists as a highly dispersed amorphous state. This result agrees well with above description that Se exists as linear shape in the 0.4~0.55 nm micropores. The structure features of the pure carbon sponge, pristine bulk Se, NCS/Se composites are further probed by Raman spectroscopy. As is shown in Fig. 3c, two strong peaks located at 1350 cm^{-1} and 1580 cm^{-1} are assigned to the D band and G band,[32, 33] respectively, revealing the partially graphitized nature of the as-synthesized layered NCS. For the pristine Se, there exist three peaks located at 142, 235 and 458 cm^{-1}. However, after Se is infused into the NCS, all the characteristic peaks disappear. It is previously reported that Se confined in mesopores[12, 14] and 1.1 nm micropores [30] exhibits peaks located at 262 cm^{-1} and 255cm^{-1}, respectively. The present Raman result of NCS/Se-50 composite indicates that there may be difference for the existence state of Se from previous works. This result further confirms that Se exists as highly dispersed amorphous linear shape in the 0.4~0.55 nm micropores.

The X-ray photoelectron spectroscopy (XPS) is used to characterize the chemical composition and chemical bonding state of the NCS/Se-50 composite. Fig. 3d shows XPS survey spectra of NCS-50 composite, several peaks can be observed. The peaks located at 229.9, 161.7 and 55.7 eV, correspond to Se 3s, Se 3p and Se 3d, respectively. Peaks at 532.0, 398.9 and 284.7 eV, correspond to O 1s, N 1s and C 1s, respectively. This result confirms the presence of Se, C, O and N elements in the composite. In the Se 3d spectrum (Fig. 3e), two fitted

peaks located at 56.2 and 55.4 eV are assigned to Se $3d_{3/2}$ and Se $3d_{5/2}$ due to spin orbit coupling[34]. The N 1s spectrum (Fig. 3f) is fitted into three peaks at 398.4 eV, 400.0 eV and 401.7 eV, corresponding to pyridinic N (N_1), pyrrolic N (N_2) and graphitic N (N_3), respectively. N_1 and N_2 atoms that are considered to be able to improve the surface adsorption towards S and polysulfide species in previous study[17], may also have the same effect on Se species. N_3 atoms are proved to be the presence of more free electrons, thus providing more unhindered pathway for electrons during delithiation-lithiation processes[35].

Cathodes are prepared using NCS/Se composites and then paired with lithium metal foils as anodes. Carbonate electrolyte is used because of the absence of lithium polyselenides during discharge-charge processes[36]. The SEI film is easily formed in the carbonate electrolyte during the first discharge process, which can also serve as a protective layer for the active material to ensure cycling stability[14, 15]. So 1.0 M $LiPF_6$ mixed with EC and DEC (1:1 by volume) is used as electrolyte. For a comparison, non-nitrogen-doped CS/Se-50 and CS/Se-60 composites with incorporated 50 and 60 wt.% Se content, respectively, are used to investigate the effect of nitrogen doping on electrochemical performance.

Cyclic voltammogram (CV) curves of the NCS/Se-50 composite cathode are shown in Fig. 4a in the voltage range of 3.0 V~1.0 V at a constant scan rate of 0.1 mV s^{-1}. As is shown, only one pair of redox peaks are observed, indicating only single phase-transition reaction during discharge-charge processes. One broad cathodic peak located between 1.7 V-1.9 V observed during the first cathodic scan, corresponds to the transformation from Se to Li_2Se, as well as the formation of solid electrolyte interface (SEI) layer. In the subsequent cycles, the cathodic peak keeps stable at 1.75 V with relatively smaller peak area, revealing the irreversible formation of SEI layer, which is the main reason of relatively low irreversible capacity during the initial cycle. The anodic peak at 2.25 V is due to the formation of Se.[37] The subsequent CV curves overlap well with each other, demonstrating a good cycling stability during the subsequent cycles.

Galvanostatic discharge-charge experiments are carried out to evaluate the lithium storage properties of the NCS/Se samples at a current density of 0.5 C (1 C = 675 mAg^{-1}) in a voltage range of 3.0 V~1.0 V at 25 ºC. Fig. 4b shows the discharge/charge profiles for different cycles of NCS/Se-50 sample. As is shown, a long discharge plateau starts at 2.0 V and finally ends up at 1.6 V, corresponding to a high initial discharge capacity of 982.6 mAh g^{-1} and an initial capacity of 584.3 mAh g^{-1}. The irreversible capacity during the first cycle is mainly due to the formation of SEI film. In the subsequent cycles, the cathode exhibits a stable discharge plateau at 1.75 V, corresponding to the lithiation processes of selenium. The discharge/charge profiles of 10^{th}, 50^{th} and 100^{th} almost overlap with each other, demonstrating a stable electrochemical performance of the NCS/Se-50 cathode.

Fig. 4c displays the cycling performance of the NCS/Se-50 cathode at a current density of 0.5 C (1 C = 675

mAg^{-1}) in a voltage range of 3.0~1.0 V at 25 ºC. The cycle performance of NCS/Se-50, -60 and CS/Se composites without nitrogen doping is comparatively investigated to study the influence of the nitrogen doping and the amount of selenium incorporated in the composites. The initial discharge/charge capacity of NCS/Se-50 and CS/Se-50 are 982.6/584.3 and 898.8/610.2 mAh g^{-1}, respectively. For the NCS/Se-50 cathode, the capacity shows a slow decrease in the following 4 cycles, finally reaching 471.6 mAh g^{-1} with a coulombic efficiency of 97.2% at the 5^{th} cycle. Then it shows perfect stability in the subsequent cycles, exhibiting 443.2 mAh g^{-1} at 200^{th} cycle with a coulombic efficiency up to 99.9%. This corresponds to 0.031% capacity loss per cycle during 5^{th} to 200^{th} cycle. For the CS/Se-50 cathode, it exhibits 452.5 and 352.2 mAh g^{-1} at 5^{th} and 200^{th} cycle, respectively, showing a continuous slow decrease of capacity, indicating a continuous slow loss of active material. The NCS/Se-50 composite with nitrogen doping not only provides a faster charge transfer passway but also shows stronger confinement ability for selenium, resulting in better electrochemical performance. For the NCS/Se-60 cathode, its initial discharge and charge capacity is 857.8 and 485.4 mAh g^{-1}, respectively. The discharge capacity is maintained at 400.6 mAh g^{-1} at 40^{th} cycle. However, it exhibits a continuous capacity fading in the subsequent cycles, maintaining only at a value of 347.7 mAh g^{-1} at 200^{th} cycle. The continuous capacity fading may be due to the continuous loss of relatively unstable selenium at the mesopore channels. This is consistent with the TGA results. In the NCS/Se-60 cathode, micropores are totally blocked and more mesoporoes are occupied according to the BET results. So no redundant space is left for buffering the volume changes of selenium and for the passage of electrolyte. This should be another reason for its lower capacity and continuous capacity fading. As a striking contrast, the capacity of CS/Se-60 cathode drops quickly after 20 cycles and finally retains only at 136.7 mAh g^{-1} at 200^{th} cycle.

The rate capability of NCS/Se and CS/Se composites cathodes is investigated under various current densities from 0.1 C to 5 C, as illustrated in Fig. 4d. For the NCS/Se-50 cathode, it exhibits a discharge of 605 mAh g^{-1} at a current density of 0.1 C in the first 10 cycles. Then the capacity of 575.9 and 513.4 mAh g^{-1} is achieved at 0.2 C after 20 cycles and 0.5 C after 30 cycles, respectively. Further increasing the current density to 1 C and 2C, the discharge capacity of 456.9 and 392.6 mAh g^{-1} is maintained after 40 and 50 cycles, respectively. Even at a high rate of 5 C after 60 cycles, the capacity can still maintain at 286.6 mAh g^{-1}. When the current density is back to 0.1 C, the capacity recovers back to 594.6 mAh g^{-1}, revealing a good high rate performance of NCS/Se-50 cathode. For the NCS/Se-60 cathode, it can exhibit 207.2 mAh g^{-1} at 5 C. The relatively worse rate capability may result from a relatively low utilization of active material whose micropores are totally blocked, especially at high rates. For the non-nitrogen-doped CS/Se-50 and CS/Se-60 composite, the discharge capacity of 183.7 and 139.9 mAh g^{-1} is achieved at 5 C after 60 cycles, respectively, accompanied with a continuous capacity loss during cycles.

The capacities of NCS/Se cathodes at high rate 5 C are much better than that of CS/Se cathodes, further confirming the enhancement of nitrogen doping on electrochemical performance.

The electrochemical impedance spectroscopy (EIS) is conducted to demonstrate the Nyquist profiles of AC impedance for NCS/Se-50 and CS/Se-50 cathode after different discharge-charge cycles (1^{st}, 10^{th}, 50^{th} and 100^{th}), as shown in Fig. 5. Each plot consists of a semicircle in the high-frequency region that is attributed to the charge transfer process, and a sloping line in the low-frequency region that is related to the mass transfer of lithium ions. For the NCS/Se-50 cathode (Fig. 5a), the Nyquist profiles of 10^{th}, 50^{th} and 100^{th} almost overlap with each other, indicating a stable structure of the cathode materials. The semicircle diameter of 1^{st} is much larger, indicating a higher impedence, which may result from the relatively lower electrochemical contact during the first several cycles. Compared with that of CS/Se-50 (Figure 5b), the semicircle diameter of NCS/Se-50 under the same cycle number is relatively smaller, revealing a smaller impedance of NCS/Se-50 with nitrogen doping, which may promise a better electrochemical performance.

To further confirm the structure stability of the cathode material during the discharge/charge processes, the coin cell of NCS/Se-50 cathode is disassembled after 150 cycles. The active materials are then peeled off from electrode disc and washed with deionized water and ethanol for several times. The SEM and elemental mapping results are shown in Fig. 6. It is clearly shown that the rod like morphology for the porous NCS can still be well retained after 150 discharge/charge cycles (Fig. 6b). The active NCS materials still display as rod-like sponge structures, indicating a robust structure of carbon sponge, which can accommodate the large volume change during delithiation/lithiation processes. EDX mapping result (Fig. 6c-6d) reveals a uniform distribution of selenium along the carbon sponge, demonstrating the firmly confinement of Se species in carbon matrices.

The excellent electrochemical performance of large surface area NCS with Se species firmly immobilized in micropores can be attributed to the characteristic advantages of the N-doped porous carbon sponge derived from MOF precursors. As is illustrated in Fig. 7, highly dispersed Se species are confined in 0.4~0.55 nm micropores of the Al-MOF-derived NCS through melting-diffusion method under vacuum. During the discharge and charge processes, the 0.4~0.55 nm micropores serve as a firmly immobilizer for Se species and the subsequent lithium selenides to avoid their loss and dissolution. The 5~10 nm mesopores can absorb large amount of electrolyte to ensure quick transfer of Li ions. The nitrogen-doped robust carbon sponge matrix with good electric conductivity not only facilitates charge transfer but also buffers the huge volume change, making the active material more electrochemically stable. During the first discharge process, linear selenium reacts with lithium to form Li_2Se. Protective SEI film is formed in the carbonate electrolyte in the 1^{st} discharge process also ensure a stable electrochemical environment in following cycles, thus leading to a stable electrochemical performance.

4. Conclusions

In summary, a nitrogen-doped layered carbon sponge (NCS) is successfully synthesized by carbonization of MOF precursor under Ar and NH_3 flow. Selenium is firmly confined within micropores of carbon layers by a melting-diffusion method. When evaluated as cathode materials for Li-Se batteries, the NCS/Se-50 composite can exhibit capacity of 443.2 mAh g^{-1} at 200th cycle with a coulombic efficiency up to 99.9% at a current density of 0.5 C, corresponding to 0.031% capacity loss per cycle during 5th to 200th cycle. Furthermore, it can even retain a capacity of 286.6 mAh g^{-1} at 5 C after 60 cycles, revealing excellent cycle performance and rate capability. The robust carbon sponge materials provide an ultrastable electrochemical environment for delithiation-lithiation processes of selenium: (1) Micropres in the carbon layers behave as an efficient immobilizer for linear selenium to avoid its escaping. (2) Mesopores between carbon layers not only serve as electrolyte absorber to ensure sufficient contact between active materials and electrolyte, but also act as cushion space to buffer the large volume changes during cycles. (3) Nitrogen doping further facilitates electron transfer, leading to a better electrochemical performance, especially at high rates. The unique microstructure of this NCS makes it an excellent immobilizer of selenium for Li-Se batteries and NCS derived from Al-MOFs can be further applied in other energy storage devices.

Acknowledgements

We acknowledge support from the National Natural Science Funds for Distinguished Young Scholars (No.: 51025211), National Nature Science Foundation of China (No.: 51472148, 51272137), the Tai Shan Scholar Foundation of Shandong Province.

References

[1] M. Armand, J.-M. Tarascon.Building better batteries. Nature **2008**, 451, 652-657.

[2] L. Shen, E. Uchaker, X. Zhang, G. Cao.Hydrogenated $Li_4Ti_5O_{12}$ nanowire arrays for high rate lithium ion batteries. Adv Mater **2012**, 24, 6502-6506.

[3] Y. K. Sun, S. T. Myung, B. C. Park, J. Prakash, I. Belharouak, K. Amine.High-energy cathode material for long-life and safe lithium batteries. Nat Mater **2009**, 8, 320-324.

[4] J. Y. Luo, W. J. Cui, P. He, Y. Y. Xia.Raising the cycling stability of aqueous lithium-ion batteries by eliminating oxygen in the electrolyte. Nat Chem **2010**, 2, 760-765.

[5] P. Barpanda, M. Ati, B. C. Melot, G. Rousse, J. N. Chotard, M. L. Doublet, M. T. Sougrati, S. A. Corr, J. C. Jumas, J. M. Tarascon.A 3.90 V iron-based fluorosulphate material for lithium-ion batteries crystallizing in the triplite structure. Nat Mater **2011**, 10, 772-779.

[6] A. Magasinski, P. Dixon, B. Hertzberg, A. Kvit, J. Ayala, G. Yushin.High-performance lithium-ion anodes using a hierarchical bottom-up approach. Nat Mater **2010**, 9, 353-358.

[7] P. G. Bruce, S. A. Freunberger, L. J. Hardwick, J. M. Tarascon.Li-O2 and Li-S batteries with high energy storage. Nat Mater **2012**, 11, 19-29.

[8] Y. Yang, G. Zheng, Y. Cui.Nanostructured sulfur cathodes. Chem Soc Rev **2013**, 42, 3018-3032.

[9] J. Shim, K. A. Striebel, E. J. Cairns.The Lithium/Sulfur Rechargeable Cell. Journal of The Electrochemical Society **2002**, 149, A1321-A1325.

[10] X. Ji, L. F. Nazar.Advances in Li–S batteries. Journal of Materials Chemistry **2010**, 20, 9821-9826.

[11] A. Abouimrane, D. Dambournet, K. W. Chapman, P. J. Chupas, W. Weng, K. Amine.A new class of lithium and sodium rechargeable batteries based on selenium and selenium-sulfur as a positive electrode. J Am Chem Soc **2012**, 134, 4505-4508.

[12] C. Yang, S. Xin, Y. Yin, H. Ye, J. Zhang, Y. Guo.An Advanced Selenium-Carbon Cathode for Rechargeable Lithium-Selenium Batteries. Angew Chem Int Ed Engl **2013**, 52, 8363-8367.

[13] Y. Cui, A. Abouimrane, J. Lu, T. Bolin, Y. Ren, W. Weng, C. Sun, V. A. Maroni, S. M. Heald, K. Amine.(De)lithiation mechanism of Li/SeS(x) (x = 0-7) batteries determined by in situ synchrotron X-ray diffraction and X-ray absorption spectroscopy. J Am Chem Soc **2013**, 135, 8047-1856.

[14] C. Luo, Y. Xu, Y. Zhu, Y. Liu, S. Zheng, Y. Liu, A. Langrock, C. Wang.Selenium@Mesoporous Carbon Composite with Superior Lithium and Sodium Storage Capacity. ACS NANO **2013**, 7, 8003-8010.

[15] Z. Li, L. Yuan, Z. Yi, Y. Liu, Y. Huang.Confined selenium within porous carbon nanospheres as cathode for advanced Li–Se batteries. Nano Energy **2014**, 9, 229-236.

[16] X. G. Sun, X. Wang, R. T. Mayes, S. Dai.Lithium-sulfur batteries based on nitrogen-doped carbon and an ionic-liquid electrolyte. ChemSusChem **2012**, 5, 2079-2085.

[17] J. Yang, J. Xie, X. Zhou, Y. Zou, J. Tang, S. Wang, F. Chen, L. Wang.Functionalized N-Doped Porous Carbon Nanofiber Webs for a Lithium–Sulfur Battery with High Capacity and Rate Performance. The Journal of Physical Chemistry C **2014**, 118, 1800-1807.

[18] J. Song, T. Xu, M. L. Gordin, P. Zhu, D. Lv, Y.-B. Jiang, Y. Chen, Y. Duan, D. Wang.Nitrogen-Doped Mesoporous Carbon Promoted Chemical Adsorption of Sulfur and Fabrication of High-Areal-Capacity Sulfur Cathode with Exceptional Cycling Stability for Lithium-Sulfur Batteries. Advanced Functional Materials **2014**, 24, 1243-1250.

[19] H. L. Jiang, B. Liu, Y. Q. Lan, K. Kuratani, T. Akita, H. Shioyama, F. Zong, Q. Xu.From metal-organic framework to nanoporous carbon: toward a very high surface area and hydrogen uptake. J Am Chem Soc **2011**, 133, 11854-11857.

[20] W. Chaikittisilp, M. Hu, H. Wang, H. S. Huang, T. Fujita, K. C. Wu, L. C. Chen, Y. Yamauchi, K. Ariga.Nanoporous carbons through direct carbonization of a zeolitic imidazolate framework for supercapacitor electrodes. Chem Commun (Camb) **2012**, 48, 7259-7261.

[21] M. Hu, J. Reboul, S. Furukawa, N. L. Torad, Q. Ji, P. Srinivasu, K. Ariga, S. Kitagawa, Y. Yamauchi.Direct carbonization of Al-based porous coordination polymer for synthesis of nanoporous carbon. J Am Chem Soc **2012**, 134, 2864-2867.

[22] K. Xi, S. Cao, X. Peng, C. Ducati, R. V. Kumar, A. K. Cheetham.Carbon with hierarchical pores from carbonized metal-organic frameworks for lithium sulphur batteries. Chem Commun (Camb) **2013**, 49, 2192-2194.

[23] A. Comotti, S. Bracco, P. Sozzani, S. Horike, R. Matsuda, J. Chen, M. Takata, Y. Kubota, S. Kitagawa.Nanochannels of Two Distinct Cross-Sections in a Porous Al-Based Coordination Polymer. J Am Chem Soc **2008**, 130, 13664-13672.

[24] G. Cheng, B. Bonillo, R. S. Sprick, D. J. Adams, T. Hasell, A. I. Cooper.Conjugated Polymers of Intrinsic Microporosity (C-PIMs). Advanced Functional Materials **2014**, 24, 5219-5224.

[25] R. Liu, L. Wan, S. Liu, L. Pan, D. Wu, D. Zhao.An Interface-Induced Co-Assembly Approach Towards Ordered Mesoporous Carbon/Graphene Aerogel for High-Performance Supercapacitors. Advanced Functional Materials **2014**, DOI: 10.1002/adfm.201403280.

[26] Z. Li, B. Li, L. Yin, Y. Qi.Prussion blue-supported annealing chemical reaction route synthesized double-shelled Fe(2)O(3)/Co(3)O(4) hollow microcubes as anode materials for lithium-ion battery. ACS Appl Mater Interfaces **2014**, 6, 8098-8107.

[27] J. Guo, Y. Xu, C. Wang.Sulfur-impregnated disordered carbon nanotubes cathode for lithium-sulfur batteries. Nano Lett **2011**, 11, 4288-4294.

[28] K. Han, Z. Liu, H. Ye, F. Dai.Flexible self-standing graphene–Se@CNT composite film as a binder-free cathode for rechargeable Li–Se batteries. Journal of Power Sources **2014**, 263, 85-89.

[29] J. T. Lee, H. Kim, M. Oschatz, D.-C. Lee, F. Wu, H.-T. Lin, B. Zdyrko, W. I. Cho, S. Kaskel, G. Yushin.Micro- and Mesoporous Carbide-Derived Carbon-Selenium Cathodes for High-Performance Lithium Selenium Batteries. Advanced Energy Materials **2014**, DOI: 10.1002/aenm.201400981.

[30] Y. Liu, L. Si, X. Zhou, X. Liu, Y. Xu, J. Bao, Z. Dai.A selenium-confined microporous carbon cathode for ultrastable lithium–selenium batteries. J. Mater. Chem. A **2014**, 2, 17735-17739.

[31] Z. Zhang, Z. Li, F. Hao, X. Wang, Q. Li, Y. Qi, R. Fan, L. Yin.3D Interconnected Porous Carbon Aerogels as Sulfur Immobilizers for Sulfur Impregnation for Lithium-Sulfur Batteries with High Rate Capability and Cycling Stability. Advanced Functional Materials **2014**, 24, 2500-2509.

[32] J. Yang, X. Kang, L. Hu, X. Gong, S. Mu.Nanocrystalline-Li2FeSiO4 synthesized by carbon frameworks as an advanced cathode material for Li-ion batteries. Journal of Materials Chemistry A **2014**, 2, 6870-6878.

[33] B. Duong, Z. Yu, P. Gangopadhyay, S. Seraphin, N. Peyghambarian, J. Thomas.High Throughput Printing of Nanostructured Carbon Electrodes for Supercapacitors. Advanced Materials Interfaces **2014**, 1, DOI: 10.1002/admi.201300014.

[34] S. Jiang, Z. Zhang, Y. Lai, Y. Qu, X. Wang, J. Li.Selenium encapsulated into 3D interconnected hierarchical porous carbon aerogels for lithium–selenium batteries with high rate performance and cycling stability. Journal of Power Sources **2014**, 267, 394-404.

[35] M. Seredych, D. Hulicova-Jurcakova, G. Q. Lu, T. J. Bandosz.Surface functional groups of carbons and the effects of their chemical character, density and accessibility to ions on electrochemical performance. Carbon **2008**, 46, 1475-1488.

[36] Y. Cui, A. Abouimrane, C. J. Sun, Y. Ren, K. Amine.Li-Se battery: absence of lithium polyselenides in carbonate based electrolyte. Chem Commun (Camb) **2014**, 50, 5576-5579.

[37] J. Zhang, L. Fan, Y. Zhu, Y. Xu, J. Liang, D. Wei, Y. Qian.Selenium/interconnected porous hollow carbon bubbles composites as the cathodes of Li-Se batteries with high performance. Nanoscale **2014**, 6, 12952-12957.

Figure captions

Figure 1. (a-b) Low- and high-magnification FESEM images, (c-d) TEM and high-resolution TEM images, (e) XPS survey spectrum of Al-MOF derived NCS materials.

Figure 2. (a-b) FESEM images, (d-e) TEM and high-resolution TEM images, (c) (f) Se elemental mapping results of the NCS/Se-50 composites. (g) N_2 adsorption–desorption isotherms, (h) pore (>2nm) size distribution and (i) micropore size distribution of NCS and NCS/Se composites.

Figure 3. (a) TGA results of NCS/Se composites. (b) XRD patterns and (c) Raman spectra of the pure Se, NCS/Se composites and pure NCS. (d) XPS survey spectrum of NCS/Se-50. (e) Se 3d, (f) N 1s XPS spectra.

Figure 4. (a) CV curves of the NCS/Se-50 cathode for five cycles at a scan rate of 0.1 mV s^{-1} in the voltage range of 3.0-1.0 V. (b) Discharge−charge profiles of the NCS/Se-50 cathode at a current density of 0.5 C in the voltage range 3.0-1.0 V. (c) Cycling performance of NCS/Se and CS/Se composites at 0.5 C, pink circles showing the Coulombic efficiency of NCS/Se-50. (d) Rate capabilities of NCS/Se and CS/Se composites.

Figure 5. Nyquist profiles of (a) NCS/Se-50 and (b) CS/Se-50 tested after different charge times.

Figure 6. SEM images of the NCS/Se-50 electrodes (a) before cycles, (b) after 150 cycles, (c) SEM image and (d) elemental mapping results of NCS/Se active material after 150 cycles.

Figure 7. Schematic discharge-charge mechanism of the NCS/Se-50 composite cathode.

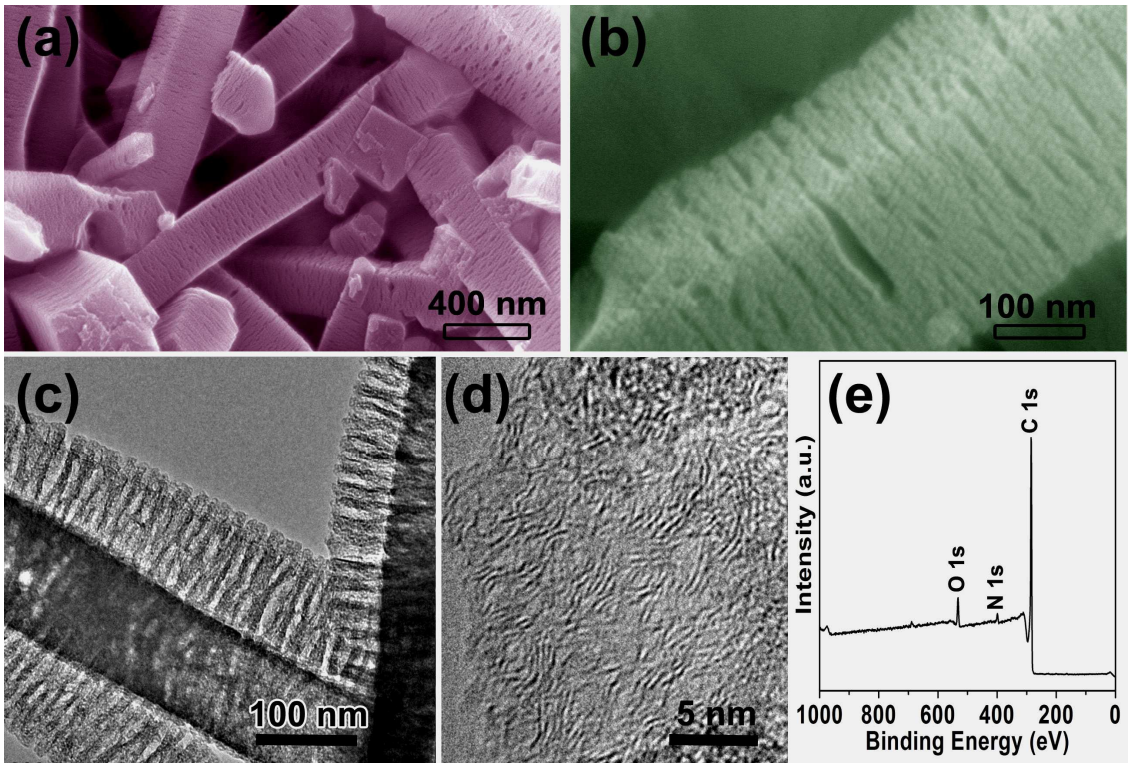

Figure 1. (a-b) Low- and high-magnification FESEM images, (c-d) TEM and high-resolution TEM images, (e) XPS survey spectrum of Al-MOF derived NCS materials.

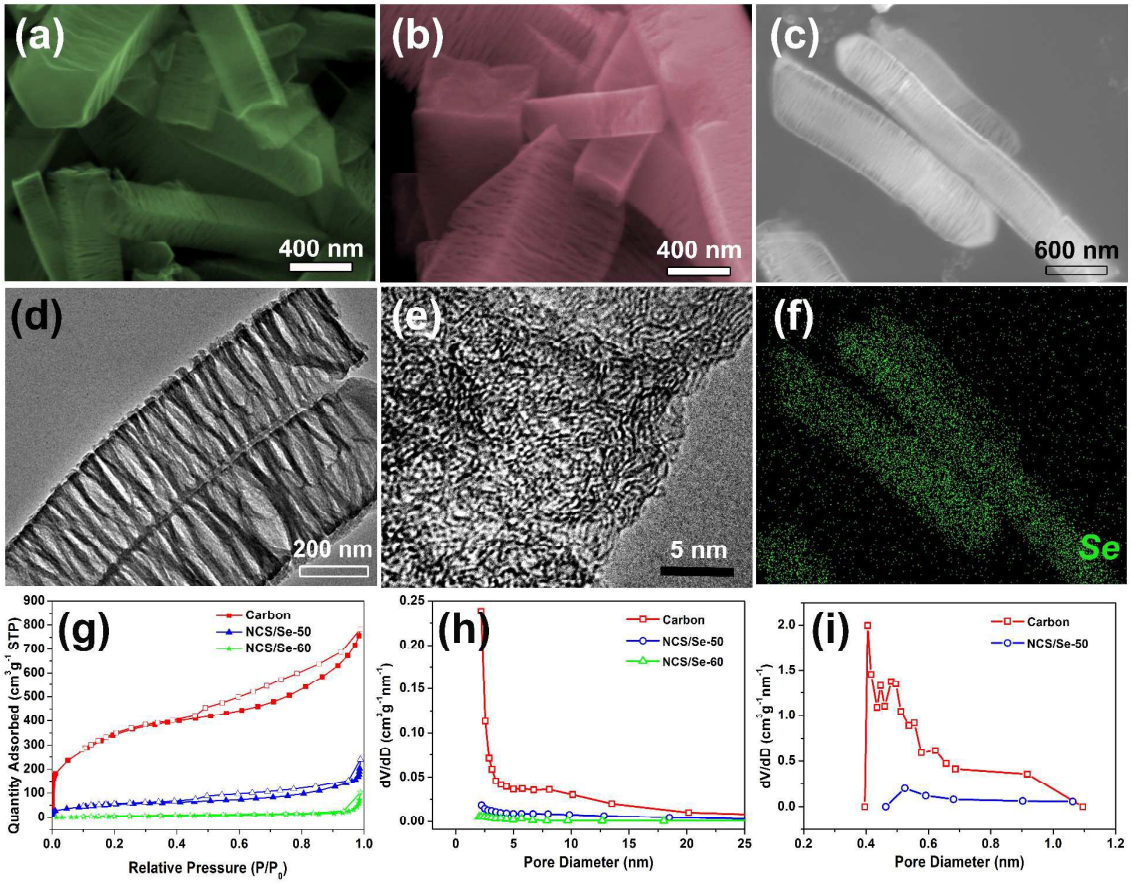

Figure 2. (a-b) FESEM images, (d-e) TEM and high-resolution TEM images, (c) (f) Se elemental mapping results of the NCS/Se-50 composites. (g) N_2 adsorption–desorption isotherms, (h) pore (>2nm) size distribution and (i) micropore size distribution of NCS and NCS/Se composites.

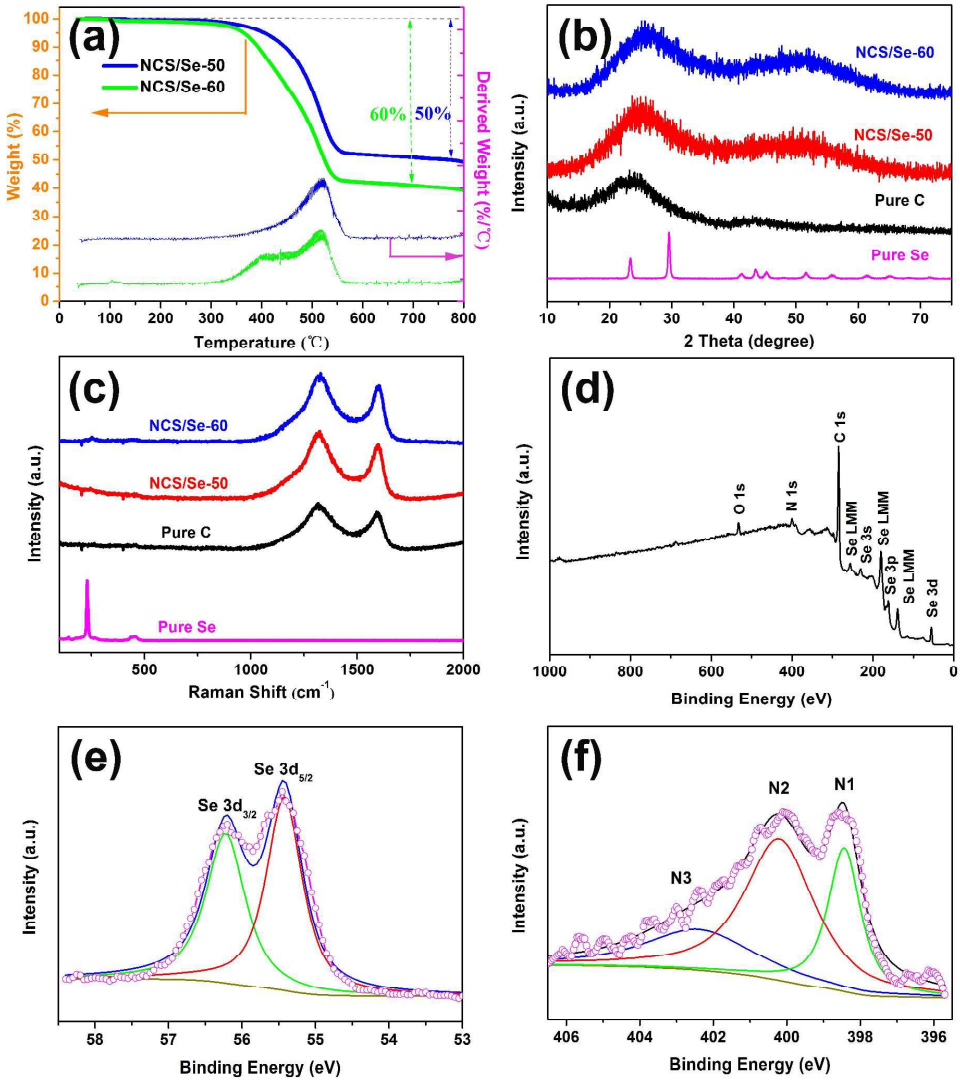

Figure 3. (a) TGA results of NCS/Se composites. (b) XRD patterns and (c) Raman spectra of the pure Se, NCS/Se composites and pure NCS. (d) XPS survey spectrum of NCS/Se-50. (e) Se 3d, (f) N 1s XPS spectra.

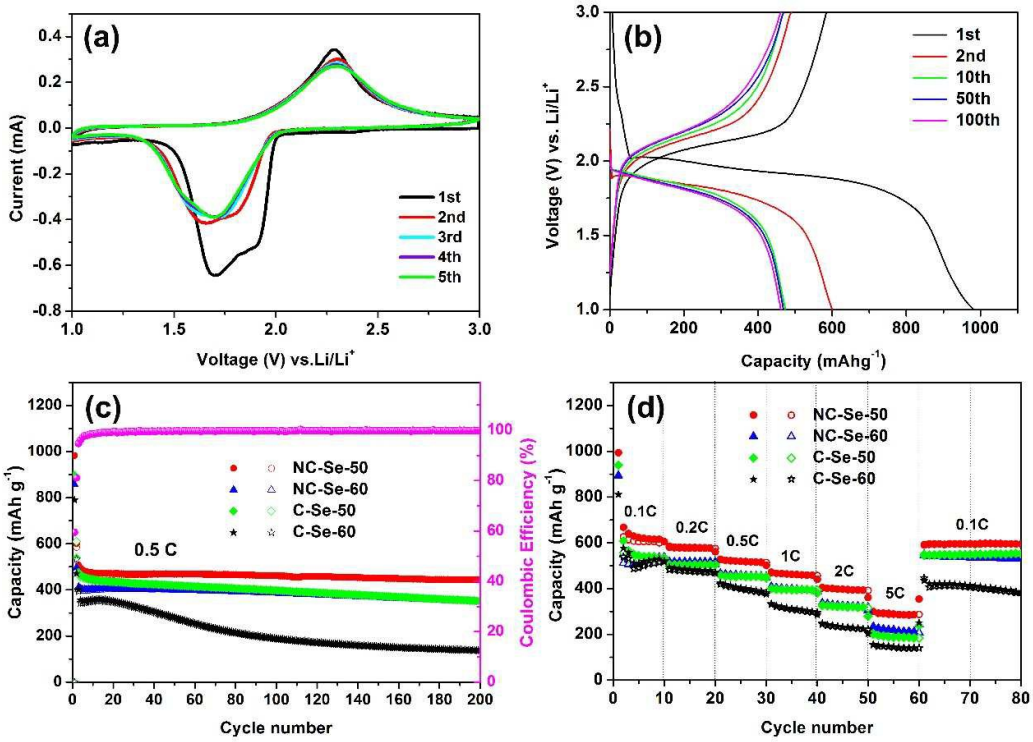

Figure 4. (a) CV curves of the NCS/Se-50 cathode for five cycles at a scan rate of 0.1 mV s^{-1} in the voltage range of 3.0-1.0 V. (b) Discharge−charge profiles of the NCS/Se-50 cathode at a current density of 0.5 C in the voltage range 3.0-1.0 V. (c) Cycling performance of NCS/Se and CS/Se composites at 0.5 C, pink circles showing the Coulombic efficiency of NCS/Se-50. (d) Rate capabilities of NCS/Se and CS/Se composites.

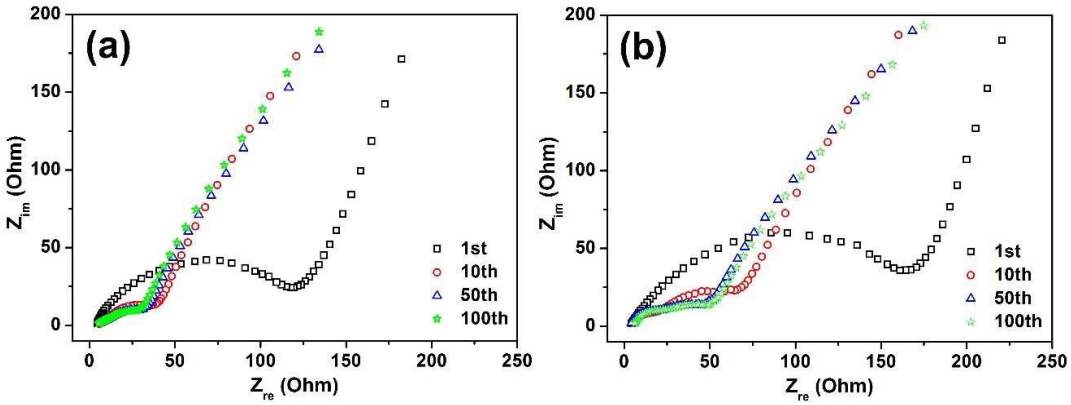

Figure 5. Nyquist profiles of (a) NCS/Se-50 and (b) CS/Se-50 tested after different charge times.

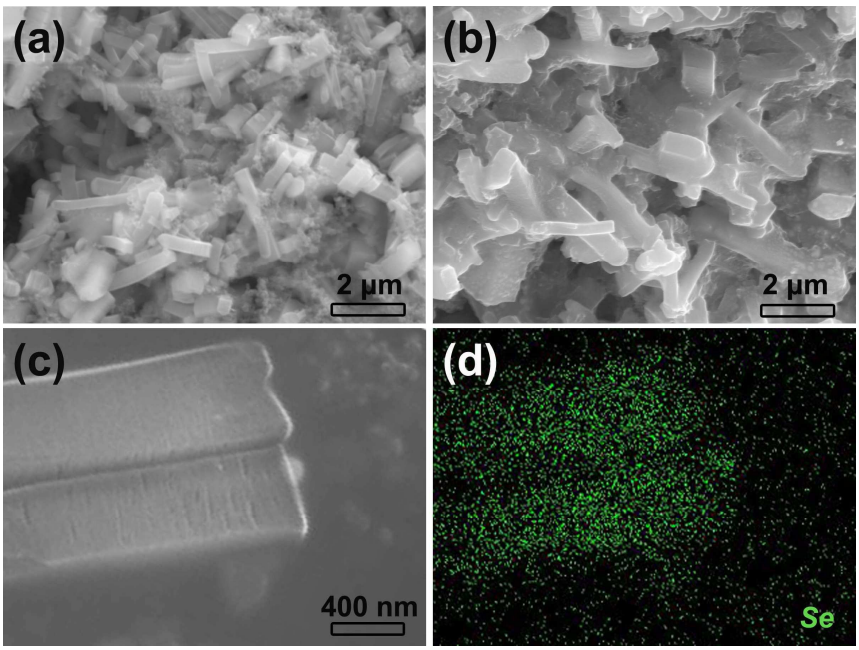

Figure 6. SEM images of the NCS/Se-50 electrodes (a) before cycles, (b) after 150 cycles, (c) SEM image and (d) elemental mapping results of NCS/Se active material after 150 cycles.

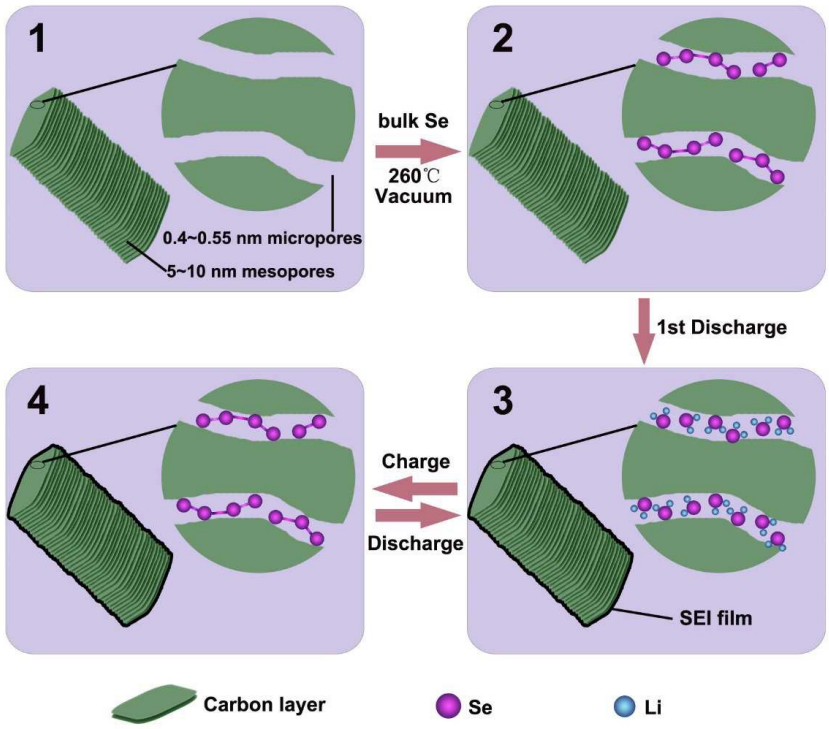

Figure 7. Schematic discharge-charge mechanism of the NCS/Se-50 composite cathode.